GSA Data Repository 2015276

Supplementary material for

First seismic evidence for continental subduction beneath the Western Alps

Liang Zhao[1]*, Anne Paul[2, 3]*, Stéphane Guillot[2, 3], Stefano Solarino[4], Marco G. Malusà[5], Tianyu Zheng[1], Coralie Aubert[2, 3], Simone Salimbeni[6], Thierry Dumont[2, 3], Stéphane Schwartz[2, 3], Rixiang Zhu[1], Qingchen Wang[1]

Computation of receiver functions and quality control

For calculation of the receiver functions, we selected events with magnitude ≥5.5 and epicentral distance between 30° and 90°. Three-component recordings of distant earthquakes were band-pass filtered (two-pole Butterworth filter) between 0.05 Hz and 0.8 Hz, and rotated into the local Z-R-T ray-based coordinate system. We then checked the data quality by computing the signal-to-noise ratio (SNR) as the ratio of the peak amplitude of the P-phase to the average amplitude across an 8-s time window prior to the onset of the P-phase. All of the P-wave records with SNR <2 on the radial component were excluded from further analysis. A first round of visual inspection was then performed to remove the remaining low-quality records.

Radial and transverse receiver functions were computed using the time-domain iterative deconvolution method (Ligorría and Ammon, 1999). A second round of visual inspection was performed, to remove low-quality receiver functions. As a result, 84 events contributed 1,647 radial receiver functions (Fig. DR1).

Figure DR2a shows the radial receiver functions selected for events with ENE back-azimuths, stacked by station, and plotted along the reference profile.

Depth migration of receiver functions

To produce a depth image beneath the receiver array, we migrated the time data to depth and stacked the radial receiver functions using the common conversion point method (Zhu, 2000). Provided that an appropriate migration velocity model is used, P-to-S (Ps)-conversions delineate layer boundaries on the migrated depth section. The three-dimensional model space beneath the array was subdivided into a three-dimensional grid of cells with bin width of 0.2 km in the vertical direction and 7 km in the horizontal direction (Fig. DR2b). Then, the radial receiver functions were back-projected from the

receiver to the source through these cells, with constant ray parameters, assuming a modified IASP91 standard Earth model (Kennett and Engdahl, 1991) with laterally variable crustal P-wave velocity along the array. The amplitude of each cell was obtained by averaging the amplitudes of the radial receiver functions of the crossing ray paths; i.e., by assigning each Ps-conversion to the location that generated it, assuming a flat-layered velocity model beneath each station. Finally, the cells located out of the reference profile (trending 73°, with middle point at 6.6°E, 44.7°N; Fig. 1, dashed line) were projected orthogonally onto the profile and stacked (Fig. DR2b). Raw migrated section were smoothed in the horizontal direction using a Gaussian operator of half-width increasing linearly with depth from 7 km (bin size) at 0 km depth to 20 km at 30 km depth. Figure DR3b shows the smoothed version of the raw CCP stack of Fig. DR2b.

The velocity model used for the time-to-depth migration was constructed based on a number of previous studies. The profile was divided into four segments with different one-dimensional migration velocity models (Table DR1). The Vp/Vs ratio was set to 1.73 in all of the layers. Although dipping interfaces are usually shifted to shallower positions with the CCP method, synthetic migration tests (Schneider et al., 2013) showed that for dipping angles smaller than 30° (which was the case in this study), the shift was negligible. This is confirmed by our two-dimensional synthetic modeling.

Effects of event back-azimuth on the CCP sections

The waveforms of the radial receiver functions strongly depend on event back-azimuth, yielding different CCP images for different ranges of back-azimuth, as shown by Figure DR3. This is due to departures from the one-dimensional velocity structure assumption that underlies the CCP migration method. Figure DR3, however, shows that the main features of the CCP section (European Moho, 'inverted Moho' of the suture zone) are well retrieved in the two ranges of back-azimuth that included a significant number of events (i.e., ENE in Fig. DR3b, NNW in Fig. DR3c). Salient differences appeared for the converted phases from the Adriatic Moho that changed geometry and depth with back-azimuth. The image of this structure might however be altered by lower signal-to-noise ratios than in other parts of the profile.

Cassidy (1992) showed that dipping interfaces generate stronger converted phases for events with up-dip incidences. As most geological structures have east to north-eastward dip, we decided to display the CCP section computed from events with ENE back-azimuths (28°-118°) in the main text. This is also the best option to attenuate out-of-plane diffracted signals due to three-dimensional structure. Finally, this selection of events in the direction of the profile is more appropriate for comparisons with the results of two-dimensional synthetic seismograms.

Two-dimensional integrated forward modeling of the CCP section

We performed a series of two-dimensional synthetic tests to test our interpretation of the CCP section that fit the Bouguer anomaly data. We focused on the modeling of the broad blue spot of negative-polarity Ps-converted phases beneath the Dora Maira massif, and on the hypothesis of subduction of the European lower crust in the Adriatic mantle.

Synthetic seismograms were first computed for different lithospheric structures using a two-dimensional hybrid numerical method (Zhao et al., 2008, 2014). The preliminary reference Earth model was used as the background model (Dziewonski and Anderson, 1981). The crustal model along the CIFALPS profile was embedded in a 1,000 km × 430 km box, inside which we used the spectral element method (Komatitsch and Tromp, 1999), and outside which we used the generalized ray theory (Wen and Helmberger, 1998). The vertical and radial components of the synthetic seismograms were calculated for 10 events at teleseismic distance, which mimicked the distribution of events used in the CCP section; i.e., with epicentral distances ranging from ~30° to 90°. In a second step, we estimated the radial receiver functions and produced a CCP image using exactly the same deconvolution method, filters, migration method, and parameters as those used for the observed dataset.

We computed the CCP sections for the crustal density models that fit the observed gravity anomaly. Density values were converted to P-wave velocity values using different empirical or experimental density–velocity relationships: the empirical linear relationship for the sediment layers ($Vp = 3.85\rho - 4.81$ with Vp in $km \cdot s^{-1}$ and ρ in 10^3 $kg \cdot m^3$; Perrier and Ruegg, 1973), the Nafe and Drake relationship for the upper and lower crust (Nafe and Drake, 1957; Ludwig, 1970), and experimental data in subduction zones for the Ivrea body and mantle layer (Christensen, 2004 ; Reynard, 2013). The Vp/Vs ratio was set to 1.73 in all of the layers. The P-wave velocity and density values in our preferred model are given in Table DR2.

For comparison, another model with a homogeneous high-velocity mantle wedge was tested (Fig. DR5). As expected, the corresponding CCP image displayed a negative signal of limited east-west extension on top and parallel to the European Moho positive conversion, much closer to the image of the continental subduction in the Pamir (6) than to our image of the West-Alpine continental subduction.

Building the western and eastern parts of the interpretative model

In the western part of the profile, we used the map of the top of the basement in the France Southeast basin (Rangin et al., 2010). The geometry of the basement was later modified to fit the Bouguer anomaly. The lower crustal thickness was set according to the ECORS-CROP deep seismic reflection data recorded in the north-western Alps (Nicolas

et al., 1990). The picked European Moho fits the Moho depth estimates from wide-angle reflection data in the [-75 km, 20 km] part of our profile (Thouvenot et al., 2007).

The Ps-conversions on the Adriatic Moho have strong amplitudes in the CCP section of Fig. 2B, but they are laterally discontinuous and their geometry and depth strongly depend on back-azimuth (Fig. DR3). The 10-km Moho jump that comes out at x = 140 km in the CCP section (Fig. 2B) is little compatible with the slowly decreasing Bouguer anomaly (Fig. 2A). Moreover, strong reverberations within the shallow low-velocity layers contaminated the Adriatic Moho signal. Thereafter, we decided to assume a smooth Adriatic Moho at a depth rising from 32 km at the eastern end of the profile, to 9 km at x = 75 km on top of the Ivrea body. We set the maximum depth of the Adriatic Moho at 30 km to 32 km, according to the MAMBo velocity model developed for the Po Plain (Molinari et al., 2015). We used the same source of information to set the depth of the other layer boundaries, the basement, and the top of the lower crust that were not imaged by the receiver function data.

After constructing the model geometry, we checked its compatibility with the Bouguer anomaly data by gravity modeling. We used a classical forward method to compute the gravity field induced at the surface by a two-dimensional model made of polygons of arbitrary density and shape (Talwani et al., 1959). The observed gravity anomaly is computed from the WGM2012 global gravity model (Balmino et al., 2012). We extracted Bouguer anomaly data in a 30-km wide stripe that followed the seismic array, and we projected the data points onto the reference profile. This provided us with an average Bouguer anomaly curve with error estimates (Fig. 2A, Fig. DR4). We then used gravity modeling to find the set of density values that fit the observed anomaly the best. The final density model and the computed and observed Bouguer anomalies are showed in Fig. DR4.

References

Balmino, G., Vales, N., Bonvalot, S. and Briais, A., 2012, Spherical harmonic modelling to ultra-high degree of Bouguer and isostatic anomalies: J. Geod., v. 86, p. 499–520.

Cassidy, J. F., 1992, Numerical experiments in broadband receiver function analysis: Bull. Seis. Soc. Am., v. 82, p. 1453-1474.

Christensen, N. I., 2004, Serpentinites, peridotites, and seismology: Int. Geol. Rev., v. 46, p. 795-816.

Dziewonski, A. and Anderson, D., 1981, Preliminary reference Earth model: Phys. Earth. Planet. Int., v. 25, p. 297-356.

Kennett, B. L. N. and Engdahl, E. R., 1991, Travel-times for global earthquake location and phase identification: Geophys. J. Int., v. 105, p. 429-465.

Komatitsch, D. and Tromp, J., 1999, Introduction to the spectral element method for the three-dimensional seismic wave propagation: Geophys. J. Int., v. 139, p. 806-822.

Ligorría, J. and Ammon, C. J., 1999, Iterative deconvolution and receiver-function estimation: Bull. Seis. Soc. Am., v. 89, p. 1395-1400.

Ludwig, J. W., Nafe, J. E. and Drake, C. L., 1970, Seismic refraction in Waxwell, A.E., ed., The Sea, Volume 4: Wiley, New York, p. 53-84.

Molinari, I., Argnani, A., Morelli, A. and Basini, P., 2015, Development and testing of a 3D seismic velocity model of the Po Plain sedimentary basin, Italy: Bull. Seis. Soc. Am. in press.

Nafe, J. and Drake, C. L., 1957, Variation with depth in shallow and deep water marine sediments of porosity, density and the velocities of compressional and shear waves: Geophysics, v. 22, p. 523-552.

Perrier, G. and Ruegg, J. C., 1973, Structure profonde du Massif Central Français: Ann. Geophys., v. 29, No. 4, p. 435-502.

Rangin, C., Le Pichon, X., Hamon, Y., Loget, N. and Crespy, A., 2010, Gravity tectonics in the SE Basin (Provence, France) imaged from seismic reflection data: Bull. Soc. Géol. Fr., v. 181, p. 503-530.

Talwani, M., Worzel, J. L. and Landisman, M., 1959, Rapid gravity computations for two-dimensional bodies with application to the Mendocino submarine fracture zone: J. Geophys. Res., v. 64, p. 49-59.

Thouvenot F. et al., 2007, Are there really superposed Mohos in the southwestern Alps? New seismic data from fan-profiling reflections: Geophys. J. Int., v. 170, p. 1180-1194.

Wen, L. and Helmberger, D., 1998, A two-dimensional P-SV hybrid method and its application to modeling localized structures near the core-mantle boundary: J. Geophys. Res., v. 103, p. 17901-17918.

Zhao, L., Zhao, M. and Lu, G., 2014, Upper mantle seismic anisotropy beneath a convergent boundary: SKS waveform modeling in central Tibet: Science China: Earth Science, v. 57, p. 759-776.

Zhao, L., Wen, L., Chen, L. and Zheng, T. Y., 2008, A two-dimensional hybrid method for modeling seismic wave propagation in anisotropic media: J. Geophys. Res., v. 113, B12307, doi:10.1029/2008JB005733.

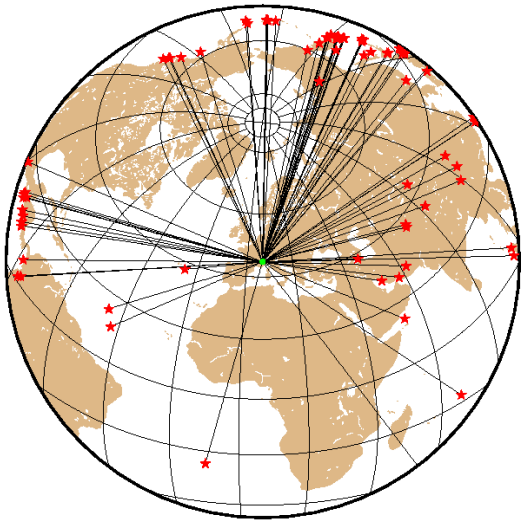

Figure DR1. Locations of events (red stars) used in the receiver function analysis. Green square, location of the study area. Most events had NNW to E back-azimuths.

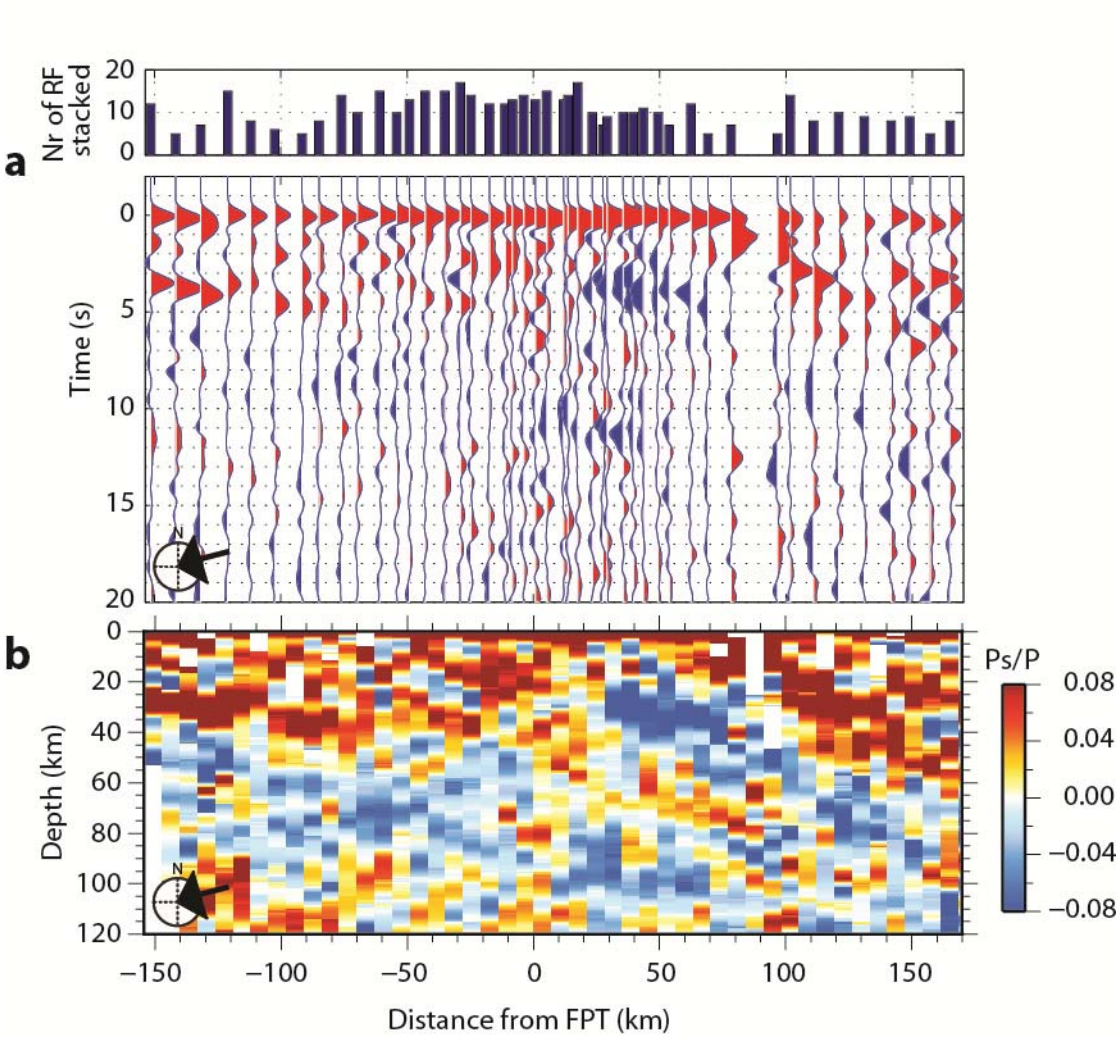

Figure DR2. Receiver function raw stacks. (a) Time traces of radial receiver functions stacked by station and plotted at the location of the station along the reference profile. The number of individual receiver functions stacked for each station is given in the bar plot (top). (b) Raw migrated CCP depth section (without horizontal smoothing). We only stacked receiver functions corresponding to ENE back-azimuths (28°-118°, indicated by the arrow).

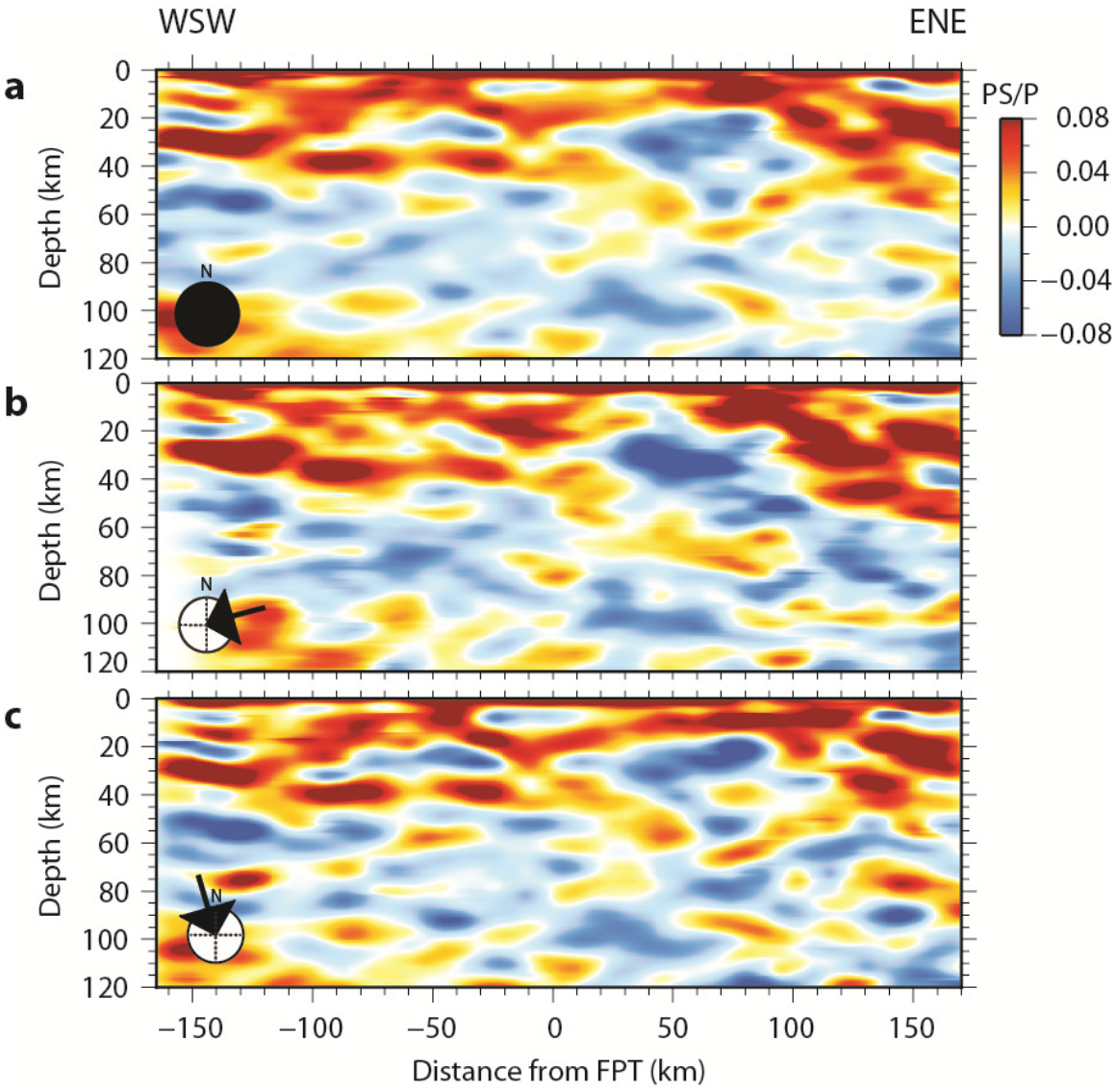

Figure DR3. CCP depth sections computed for events with different ranges of back-azimuth. (a) All back-azimuths (indicated by the black circle). (b) ENE back-azimuths (28°-118°, indicated by the arrow). (c) NNW back-azimuths (298°-28°, indicated by the arrow). The amplitude scale (indicated by the color scale in A) is the same for the 3 sections.

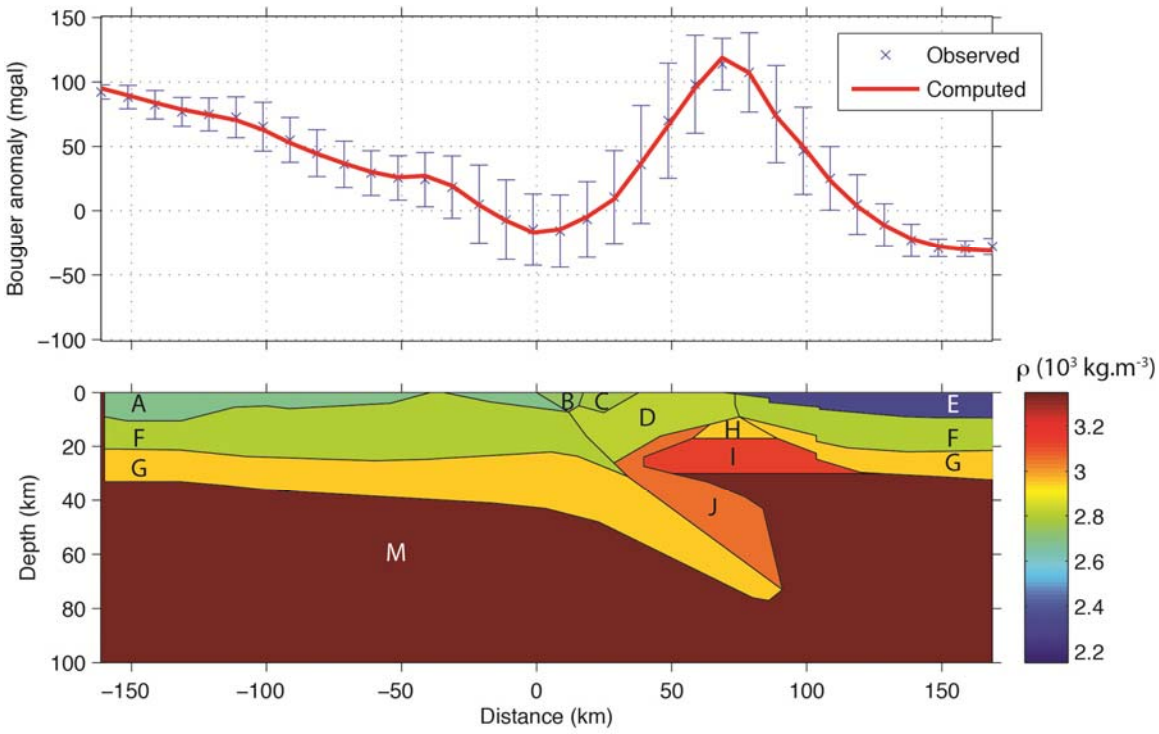

Figure DR4. Best-fit gravity model (bottom), with observed (blue markers with error bars) and computed (red curve) gravity anomalies (top). Letter codes refer to Table DR2.

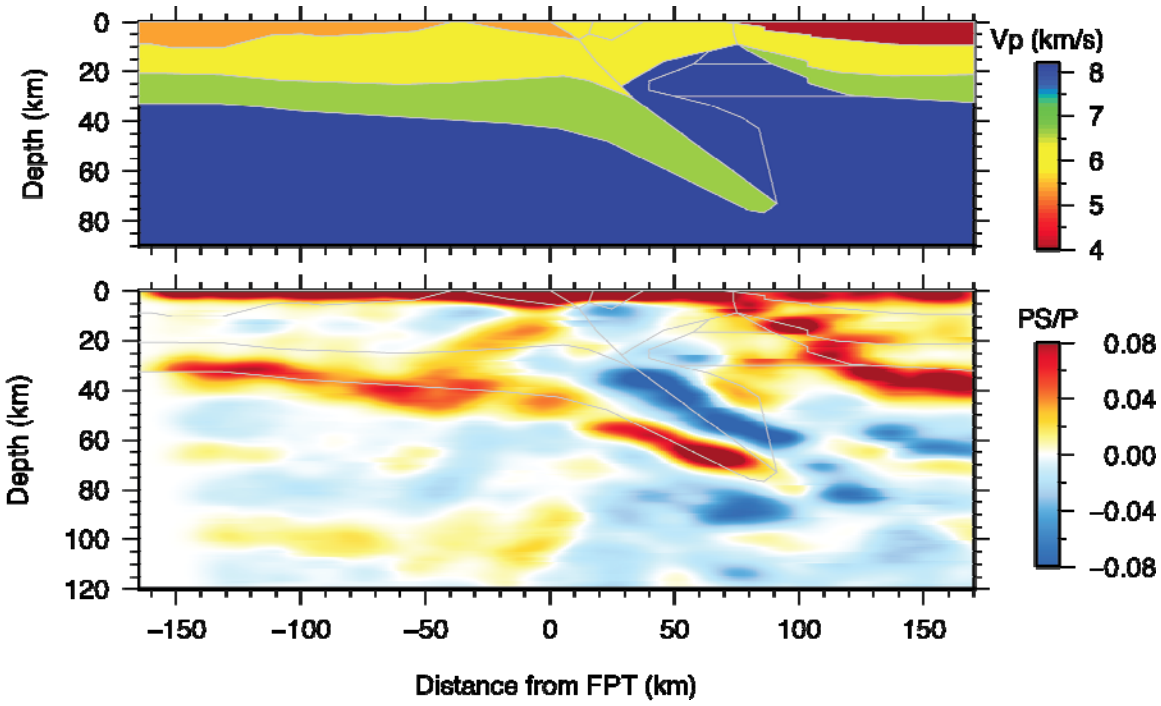

Figure DR5. Synthetic CCP depth section (bottom) computed for a crustal model where a homogeneous mantle wedge (Vp = 8.2 km·s^{-1}) replaces the Ivrea body and the wedge of UHP metamorphic rock (top).

Table DR1. Crustal velocity model used for the time-to-depth migration of the receiver functions. Vp, P-wave velocity; H, thickness.

Layer	-150 to -50 km (Southeast basin)		-50 to 15 km (External Alps)		15 to 80 km (Internal Alps)		80 to 165 km (Po basin)	
	Vp ($km \cdot s^{-1}$)	H (km)	Vp ($km \cdot s^{-1}$)	H (km)	Vp ($km \cdot s^{-1}$)	H (km)	Vp ($km \cdot s^{-1}$)	H (km)
1	5.0	5	5.5	2	5.5	2	4.1	10
2	6.0	15	6.1	18	5.8	10	6.0	11
3	6.8	25	6.8	35	7.2	24	6.8	24
4	-	-	-	-	6.8	44	-	-

Table DR2. Velocities and densities of our preferred model (Fig. 2c). Letter codes refer to Fig. DR4.

Letter code	Layer	Vp ($km \cdot s^{-1}$)	ρ ($10^3 kg \cdot m^{-3}$)
A	Southeast basin and Ubaye nappes	5.385	2.65
B	Briançonnais	5.77	2.70
C	Schistes lustrés	5.91	2.73
D	Dora Maira	6.09	2.77
E	Po basin	4.0	2.29
F	Upper crust	6.0	2.75
G	Lower crust	6.6	2.90
H	Shallow part of Ivrea body	7.4	2.90
I	Deep part of Ivrea body	7.9	3.1
J	Deep part of UHP-HP metamorphic wedge	7.02	3.02
M	Mantle	8.2	3.3